J. Fluid Mech. (2008), *vol.* 594, *pp.* 341–368.
doi:10.1017/S0022112007009172 Printed in the United Kingdom

Influence of wing kinematics on aerodynamic performance in hovering insect flight

FRANK M. BOS[1], D. LENTINK[2,1], B. W. VAN OUDHEUSDEN[1] AND H. BIJL[1]

[1]Department of Aerospace Engineering, Delft University of Technology, Kluyverweg 2, PO. Box 5058, Delft, the Netherlands
f.m.bos@tudelft.nl

[2]Wageningen University, Marijkeweg 40, PO. Box 338, Wageningen, the Netherlands

(Received 26 June 2006 and in revised form 6 September 2007)

The influence of different wing kinematic models on the aerodynamic performance of a hovering insect is investigated by means of two-dimensional time-dependent Navier–Stokes simulations. For this, simplified models are compared with averaged representations of the hovering fruit fly wing kinematics. With increasing complexity, a harmonic model, a Robofly model and two more-realistic fruit fly models are considered, all dynamically scaled at $Re = 110$. To facilitate the comparison, the parameters of the models were selected such that their mean quasi-steady lift coefficients were matched. Details of the vortex dynamics, as well as the resulting lift and drag forces, were studied.

The simulation results reveal that the fruit fly wing kinematics result in forces that differ significantly from those resulting from the simplified wing kinematic models. In addition, light is shed on the effect of different characteristic features of the insect wing motion. The angle of attack variation used by fruit flies increases aerodynamic performance, whereas the deviation is probably used for levelling the forces over the cycle.

1. Introduction

In the past, several studies that considered the flight performance of insects have revealed the complex nature of insect flight aerodynamics. The flow induced by the motion of insect wings is highly unsteady and vortical, as visualized by Weish-Fogh & Jensen (1956) using tethered locusts. More recently, Srygley & Thomas (2002) performed free-flight experimental visualizations using butterflies and showed vortical structures. This unsteady and vortical flow behaviour is a consequence of the high relative frequencies and amplitudes, and the very low Reynolds numbers involved ($Re < 1000$ for a large number of insects and $Re \approx 110$ for the fruit fly, *Drosophila Melanogaster*, in particular).

Ellington (1984) indicated that the lift in insect flight is significantly higher than expected on the basis of quasi-steady aerodynamics, revealing that important unsteady flow phenomena play a major role in insect flight. In several studies (Dickinson & Götz 1993; Dickinson 1994; Ellington *et al.* 1996) it was confirmed that the most important aspect of insect aerodynamics is the existence of the leading-edge vortex (LEV). It was shown that the LEV arises during the translational part of the wing motion rather than during the rotational flip between up- and downstroke. The

lift-increasing effect of the LEV strongly depends on the kinematics of the flapping wing (Dickinson, Lehmann & Sane 1999; Wang 2000*b*; Sane & Dickinson 2001, 2002). Besides the LEV, the lift is also enhanced due to rotational lift and wake capture (Dickinson *et al.* 1999).

In order to understand insect flight performance Dickinson *et al.* (1999) and Wang (2000*b*) applied the quasi-steady theory to compare with unsteady forces. The quasi-steady approach was revised by Sane & Dickinson (2002) to include rotational effects but still the results required further improvement. According to Sane & Dickinson (2001) the mean lift is predicted well by quasi-steady theory, but the mean drag is underestimated. This confirms the restricted applicability of the quasi-steady theory due to the lack of unsteady mechanisms such as rotational lift and wake capture.

Several experimental studies have been performed with the aim of characterizing the unsteady aerodynamics of insect flight, using either observation of live insects, or simulations with mechanical insect models. Srygley & Thomas (2002) used tethered hawkmoths and trained butterflies, while Dickinson *et al.* (1999) investigated the flow around a flapping robofly model which moves in oil to obtain the same flow conditions as the real fruit fly encounters (reproduction of Reynolds number in particular). Notwithstanding important advances in experimental techniques for non-intrusive flow field analysis, particle image velocimetry in particular (Bomphrey *et al.* 2006), it remains difficult to capture all the relevant details of the flow using only experimental techniques. An appealing approach, therefore, is to supplement experiments with numerical flow simulations. A number of numerical studies on full three-dimensional configurations have been reported, in relation to specific insect geometries: moth (Liu & Kawachi 1998), fruit fly (Ramamurti & Sandberg 2002; Sun & Tang 2002), dragonfly (Isogai *et al.* 2004), but the computational effort involved in a three-dimensional study is at present still too demanding to permit a systematic parametric study of the major parameters involved, such as the wing planform and the flapping motion parameters. Therefore, to limit both the parametric space and the computational effort, many studies have been performed as two-dimensional simulations. The possibly restrictive applicability of two-dimensional results to true insect flight is one of the major (partially unresolved) issues in modelling of insect flight and flapping wing propulsion more generally, together with the importance of unsteady flow mechanisms, wing flexibility (FSI) and Reynolds number effects. The aim of the present investigation is to contribute to the understanding of insect aerodynamics, through the use of two-dimensional numerical flow simulations. The particular issue of interest is the impact of the wing stroke kinematics model on the aerodynamic performance, and whether specific features observed in insect flight might maximize aerodynamic performance.

The similarity and discrepancy between two- and three-dimensional flows

In a recent paper Wang, Birch & Dickinson (2004) compared three-dimensional Robofly results with two-dimensional numerical results. This showed that two-dimensional simulations are useful to obtain a better understanding of the flow features, which can then be investigated more thoroughly in three dimensions.

Both Dong *et al.* (2005) and Blondeaux *et al.* (2005) concluded that two-dimensional studies overpredict forces and performances since the energy loss, which is present in three dimensions, is not solved for. Dong *et al.* (2005) and Blondeaux *et al.* (2005) numerically investigated the wake structure behind finite-span wings at low Reynolds numbers. They observed that flapping wings with low aspect ratio generate three-dimensional vortical structures as was mentioned by Lighthill (1969).

Notwithstanding the possible discrepancy between two-dimensional and three-dimensional flow, two-dimensional analysis has often been applied to obtain insight into the aerodynamic effects of choices in kinematics, airfoil cross-section, Reynolds numbers, etc. Wang *et al.* (2004) confirmed that the similarities between two- and three-dimensional approaches are sufficient that a reasonable approximation of insect flight can be obtained using a two-dimensional approach. First, in the case of advanced and symmetric rotation the forces were found to be similar in the two-dimensional simulations and three-dimensional experiments. Secondly, it was observed that in both simulations and experiments the leading-edge vortex did not fully separate for amplitude-to-chord ratios between 3 and 5 (Dickinson & Götz 1993; Dickinson 1994). We will deal with amplitudes that are in this range.

In view of the excessive computational expense required for accurate three-dimensional simulations, and with the above justification, we will restrict the present study to two-dimensional simulations. In a two-dimensional simulation our mesh resolution can be higher than in a three-dimensional simulation, in view of the limitation of computational resources.

Influence of kinematic modelling

The relevance of (experimental or numerical) simulations of insect flight has been found to depend on how reliably true insect wing kinematics are reproduced. Wang *et al.* (2004) and Sane & Dickinson (2001) showed that the kinematic modelling significantly influences the mean force coefficients and their distribution. Additionally, Hover, Haugsdal & Triantafyllou (2004) showed that modelling the angle of attack influences the flapping foil propulsion efficiency to a large extent. This illustrates the appreciable effects that details of the wing kinematics, such as parameter values and stroke patterns, may have on flight performance. It further emphasizes the need to critically assess the influence of kinematic model simplifications.

In the literature, different kinematic models have been employed to investigate the aerodynamic features of insect flight. For example, Wang (2000*a*, *b*) and Lentink & Gerritsma (2003) numerically investigated pure harmonic translational motion with respectively small and large amplitudes. Wang (2000*a*, *b*) varied flapping amplitude and frequency and showed that for a certain parameter selection the lift is clearly enhanced. Lewin & Haj-Hariri (2003) performed a similar numerical study for heaving airfoils. Besides lift enhancement at certain reduced frequencies, they found periodic and aperiodic flow solutions which are strongly related to the aerodynamic efficiency. Lentink & Gerritsma (2003) varied airfoil shape with amplitude and frequency fixed at values representative of real fruit flies. They concluded that the airfoil choice is of minor influence, but large amplitudes lead to an increase of lift by a factor of 5 compared to static forces generated by translating airfoils. It was also shown that wing stroke models with only translational motion could not provide realistic results, so that including rotation is essential. In addition to the harmonic models with pure translation (Dickinson & Götz 1993), rotational parameters were investigated by Dickinson (1994). They varied rotational parameters and showed that axis of rotation, rotation speed and angle of attack during translation are of great importance in the force development during each stroke. Harmonic wing kinematics including wing rotation were used by Pedro, Suleman & Djilali (2003) and Guglielmini & Blondeaux (2004) in their numerical models to solve for forward flight. Both studies emphasized the importance of angle-of-attack modelling to influence the propulsive efficiency. Slightly more complex fruit fly kinematic models were used by Dickinson *et al.* (1999) and Sane & Dickinson (2001) with their Robofly. Observation of

true insect flight shows that the wing maintains a constant velocity and angle of attack during most of the stroke, with a relatively strong linear and angular acceleration during stroke reversal. This results in the typical 'sawtooth' displacement and trapezoidal angle-of-attack pattern of the Robofly kinematic model. Using these models, the effect of amplitude, deviation, angle of attack and the timing of the latter were explored.

In the present study we consider the different models from literature, both the pure harmonic and the Robofly model, in order to investigate their influence on the aerodynamics. We compare the results with more realistic fruit fly kinematics obtained from the observation of free-flying fruit flies. Instead of performing a parameter study within the scope of one kinematic model, the objective of the present study is to compare the effect of the available models as a whole. This leads to better insights into the consequences of simplifications in kinematic modelling, which is of importance to both experiments and numerical simulations. Also, it can reveal the importance of certain specific features of the stroke pattern, in relation to aerodynamic performance.

This study considers four different wing kinematic models with varying degree of complexity. These models are implemented in a general-purpose Computational Fluid Dynamics (CFD) code, which solves the Navier–Stokes equations under the assumption of incompressible flow. In brief, the first model describes the wing motion using basic harmonics as derived by Wang (2000*a*). The second model contains the kinematics implemented by Dickinson *et al.* (1999) for their Robofly at UC Berkeley (currently CalTech). The third model is a representation of the real kinematics used by a hovering fruit fly (*Drosophila Melanogaster*), based on data measured by Fry, Sayaman & Dickinson (2003). Finally, the fourth model is a slightly simplified version of the latter observed fruit fly model. All these kinematic models are dynamically scaled at a Reynolds number of $Re = 110$ which corresponds to the flight conditions of the fruit fly. In addition, these kinematic models are constructed such that their mean quasi-steady lift coefficients are comparable so that our performance comparison is justified. This basis of comparison is verified from the force results of the actual simulations.

The outline of this paper is as follows. In § 2 the computational procedure is described. The modelling of the insect parameters is discussed in § 3. The results of the numerical simulations obtained with the different kinematic models are treated in § 4 and concluding remarks are given in § 5.

2. Numerical simulation methods

The different kinematic models are implemented in a commercial flow solver which solves the governing incompressible Navier–Stokes equations on a two-dimensional computational mesh. The resulting model has been validated using stationary and moving circular cylinders and verified using harmonically moving wings.

2.1. *Flow solver and governing equations*

To simulate the flow around moving wings with predefined motions the commercial CFD solver Fluent v6.1.22 was used. The two-dimensional time-dependent Navier–Stokes equations are solved using the finite volume method, assuming incompressible flow, which is justified since the Mach number of flapping insect flight is typically $O(10^{-3})$ (see Brodsky 1994). The mass and momentum equations are solved in a fixed inertial reference frame incorporating a moving mesh following the arbitrary Lagrangian Eulerian (ALE) formulation (see Ferziger & Peric 2002). The

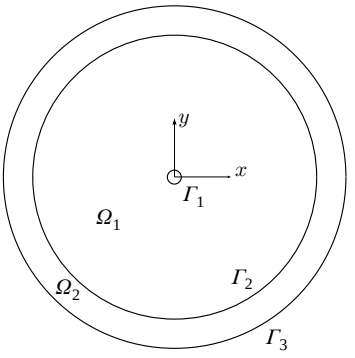

FIGURE 1. O-type mesh topology with boundary conditions on Γ_1, Γ_2 and Γ_3.

dimensionless mass and momentum conservation equations are given by

$$\nabla \cdot \boldsymbol{u} = 0, \tag{2.1a}$$

$$St\frac{\partial \boldsymbol{u}}{\partial t} + (\boldsymbol{u}\cdot\nabla)\,\boldsymbol{u} = -\nabla p + \frac{1}{Re}\nabla^2\boldsymbol{u}. \tag{2.1b}$$

Here the dimensionless flow velocity is given by $\boldsymbol{u}$ and p is the dimensionless pressure. Two main dimensionless numbers are identified as relevant parameters: the Strouhal (St) and Reynolds number (Re):

$$St = \frac{f_{ref}L_{ref}}{U_{ref}} = \frac{T_{conv}}{T_{motion}}, \tag{2.2a}$$

$$Re = \frac{U_{ref}L_{ref}}{\nu} = \frac{T_{visc}}{T_{conv}}. \tag{2.2b}$$

These dimensionless numbers represent order estimates for time-scale ratios in the flow. In (2.2) these relevant time scales are respectively the time for convective transport (T_{conv}), viscous transport (T_{visc}) and the relevant time of the body motion (T_{motion}). In order for the dimensionless numbers to have proper physical meaning, the reference values need to be chosen appropriately.

At the considered Reynolds number, $Re = O(100)$, the flow is assumed to be laminar. Henderson (1995) and Williamson (1995) showed that for circular cylinders transition from laminar to turbulent flow occurs at $Re = 180 \pm 5$, which supports this assumption. Therefore the nonstationary laminar Navier–Stokes equations (2.1) are used. Additional solver settings can be found in Appendix B.

2.2. *Mesh generation and boundary conditions*

In order to compute the flow around moving airfoils we used an O-type computational domain which is shown schematically in figure 1. The computational domain is divided into two parts: Ω_1 and Ω_2 for the inner and outer mesh respectively. The body surface Γ_1 is located in the centre of the computational domain. It has reference length L which corresponds to the wing chord length. The outer boundary Γ_3 is located at $30L$ such that the influence of the far-field boundary condition is negligible (Lentink & Gerritsma 2003). At the body surface a no-slip boundary condition is applied. Since the moving wing simulations concern hovering insect flight, such that a free stream is absent, a symmetry boundary condition was applied at Γ_3 for numerical reasons. The influence of this symmetry condition has been investigated and found to be sufficiently small.

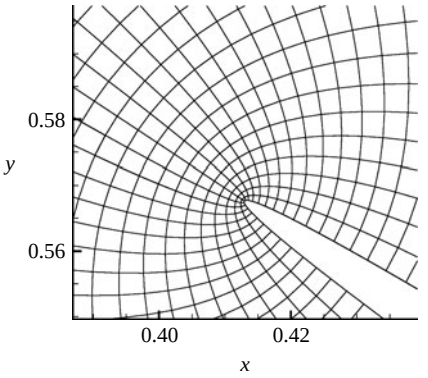

FIGURE 2. Body conformal moving mesh around a 2 % ellipsoid airfoil.

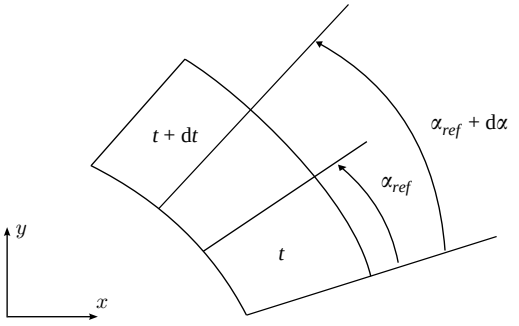

FIGURE 3. Relative cell displacement in rotation.

For the wing, which is modelled as an ellipse of 2 % thickness, generation of a high-quality mesh is not as straightforward as for a cylinder. The geometric surface gradient is high, especially at the leading and trailing edges. This complicates the creation of a high-quality mesh, i.e. high cell orthogonality. In order to create this body-conformal mesh (see figure 2) a conformal mapping was applied (see Wang 2000*b*). The intermediate interface Γ_2 divides the mesh into two separate fields, corresponding respectively to the inner conformal mesh (Ω_1) and the outer mesh (Ω_2). The complete inner mesh moves according to the wing kinematics, while re-meshing takes place in the outer field Ω_2. Since re-meshing occurs at a distance of 25 to 30 body lengths away from the wing, the flow around the wing is not affected by the mesh regeneration. The described computational setup was thoroughly validated using the flow around stationary and moving circular cylinders, see Appendix C.

The airfoil simulations were performed on a mesh of 50×10^3 cells with 2000 time steps within one motion period. With this mesh the size of the first cell at the wing surface varies between 2 % and 50 % of the wing thickness at the leading edge and in the middle of the profile respectively. The grid resolution near the wing up to 1 chord length was 8800 (176×50) cells such that the leading- and trailing-edge vortices were captured with at least 1000 cells. One run, simulating 18 flapping periods, needed approximately 10 days on one serial AMD Athlon 2500+ CPU.

In order to minimize the interpolation errors from one time step to the next it is important to analyse the influence of the relative cell displacements. We therefore investigate the motion of a reference cell which is illustrated for the rotational motion in figure 3. The relative displacements in the rotational and translational direction

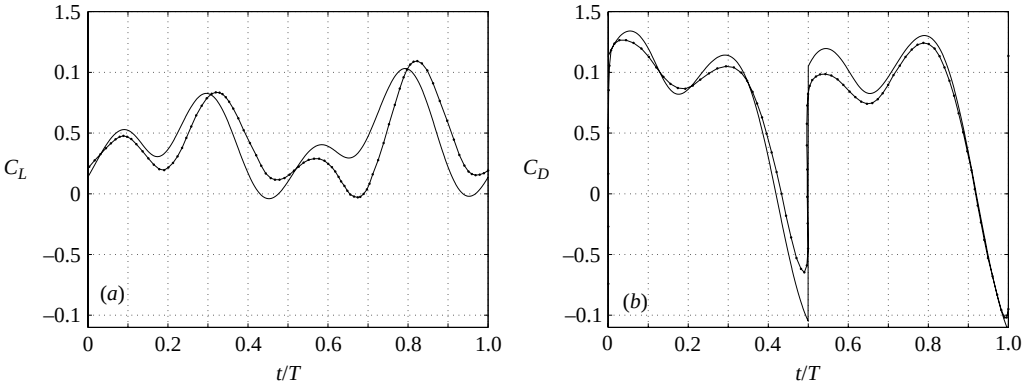

FIGURE 4. Comparison of force coefficients obtained in the present simulations (—) with Wang *et al.* (2004) (●). Harmonic wing kinematics with $A = 2.8$, $Re = 75$.

give the constraints for the size of the time step in order to keep the interpolation errors within limits. These relative displacements are defined as

$$\epsilon_r = \frac{\Delta\alpha}{\alpha_{ref}}, \tag{2.3a}$$

$$\epsilon_y = \frac{\Delta y}{y_{ref}} = \frac{2 f_e A_e N \Delta t}{y_{ref}}. \tag{2.3b}$$

Here α corresponds to the angular displacement of the reference cell, while α_{ref} is the original radial length of this cell. The linear displacement of this cell is y and y_{ref} is its original length. Furthermore, f_e, A_e and N correspond respectively to, the frequency, amplitude and number of cells on the surface.

From the validation, see Appendix C, it was found that a relative displacement of 10 % in both the rotational and translational direction leads to accurate results with differences in drag coefficients remaining below 5 %. The computational time is acceptable: 2000 time steps within one excitation period. In Appendix D the mesh and time-step independence for the nominal solver settings are investigated using harmonic wing kinematics for hovering flight.

2.3. *Validation using harmonic wing kinematics*

The main numerical parameters, a mesh size of 50×10^3 cells and 2000 time steps within one excitation period, are used to validate our results with respect to those obtained by Wang *et al.* (2004) for similar but not identical conditions. We selected a two-dimensional case with a moving wing according to harmonic kinematics. The amplitude was 2.8 times the chord length, which corresponds to $Re = 75$. Figure 4 shows the lift and drag coefficients for validation purposes. Our forces are normalized with the maximum of the quasi-steady force, as in Wang *et al.* (2004). Corresponding to Wang *et al.* (2004) the drag in figure 4 (*a*) is defined to be positive in the direction opposite to the horizontal motion.

Generally, our force distribution looks similar for both cases. Just after stroke reversal our computation obtains a larger lift and drag, which is probably the result of different numerical dissipation properties of the two codes. The mean lift and drag coefficients are 0.84, 1.47 for our simulation, compared to 0.82, 1.44 obtained by Wang *et al.* (2004), which is a difference of only 2 % and therefore we consider our computations to be sufficiently accurate. Moreover, within the context of comparing

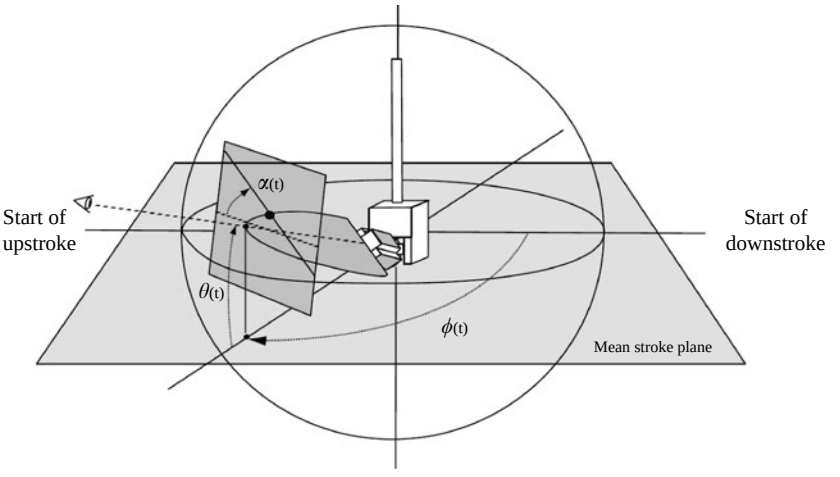

FIGURE 5. Illustration of the main motion directions. $\phi(t)$ corresponds to the stroke variation, $\alpha(t)$ to the geometrical angle of attack and $\theta(t)$ to the deviation from the horizontal stroke plane. Source: Sane & Dickinson (2001). Reproduced with permission of the Company of Biologists.

results for different stroke patterns, the present numerical method is proven to be accurate.

Further details of the validation and verification studies can be found in respectively Appendix C and D.

3. Modelling insect wing kinematics

In order to derive the two-dimensional kinematic models the three-dimensional degrees of freedom need to be converted into their two-dimensional counterparts. A common procedure is to define an equivalent two-dimensional geometry, while maintaining the characteristic aspects of the wing motion. This two-dimensional set-up is derived in § 3.1 in terms of wing selection and model parameters. The dynamical scaling and the force definitions are described respectively in § 3.2 and § 3.3.

3.1. *Insect wing selection and model parameters*

The computational approach is applied to investigate the influence of different kinematic wing motion models on the aerodynamic performance. The different kinematic models are illustrated using the Robofly experimental set-up, shown in figure 5 (see Sane & Dickinson 2001; Dickinson *et al.* 1999). In this three-dimensional model the three degrees of freedom of the wing motion are defined as: the angular displacement ϕ in the mean stroke plane, the angle of attack α with respect to the horizontal plane and the deviation from the horizontal plane θ, as is shown in figure 5. The deviation causes a 'figure-of-eight' pattern which is present in real fruit fly kinematics (see Fry *et al.* 2003). The two-dimensional airfoil shape is chosen to be a 2 % thick ellipsoid. Lentink & Gerritsma (2003) found this airfoil an acceptable choice to model insect wings at low Reynolds numbers, $Re = O(100)$. The two-dimensional projection is defined at a representative spanwise location such that the motion is confined to an arc around the wing root. Birch & Dickinson (2003) found the strongest vorticity at a spanwise location of $0.65R$ from the wing root, where R is the wing span. Therefore Wang *et al.* (2004) used this distance to derive their two-dimensional model.

In the present study we consider a different argument for the selection of the projection location (Lentink & Gerritsma 2003). As the local velocity of each cross-section varies during flapping, we select the spanwise location to be at the radius of gyration where the mean lift acts (see Ellington 1984).

To provide completeness for the three-dimensional set-up, the values used are: for the wing surface $S = 0.0167\,\mathrm{m}^2$, the radius, $R = 0.254\,\mathrm{m}$, the location of centre of gravity, $x_{cg} = 0.0882\,\mathrm{m}$, the location of the wing base, $x_{base} = 0.0667\,\mathrm{m}$ and the moment of inertia, $I_{cg} = 40.42 \times 10^{-4}\,\mathrm{m}^4$. For the radius of gyration we obtained $R_g = 0.6396\,R$. Compared to the value used by Wang *et al.* (2004) our cross-section is just less than 2 % closer to the wing root. Apparently the mean lift acts nearly at the location where the vorticity is maximal. Another important parameter to be defined is the reference length, L_{ref}, based on the mean chord length. We propose a definition of the mean chord length based on the moment of inertia around the wing root. This leads to a value for the mean chord length of $\bar{c} = 0.082\,\mathrm{m}$ Finally, the conversion from three-dimensional angles to non-dimensional displacements is given by

$$\bar{x} = \frac{\phi\, R_g}{\bar{c}}, \quad \bar{y} = \frac{\theta\, R_g}{\bar{c}}, \tag{3.1}$$

where R_g is the radius of gyration. Both the displacement $\bar{x}$ and the deviation $\bar{y}$ have been made dimensionless with the mean chord $\bar{c}$. The centre of rotation is defined at the aerodynamic centre which lies at the quarter-chord point of the mean chord.

3.2. *Dynamical scaling of the wing model*

Since the flapping of the wings induces highly unsteady flow the relevant flow and motion parameters have to be scaled dynamically. The period of the motion is used to average the relevant flow velocity (Lentink & Gerritsma 2003):

$$\overline{U} = \frac{1}{T}\int_0^T \sqrt{u^2 + v^2}\,\mathrm{d}t. \tag{3.2}$$

Here T is the period (in second), u represents the non-dimensional velocity in the stroke plane and v the non-dimensional deviation velocity, given by $u = \partial\bar{x}/\partial\bar{t}$ and $v = \partial\bar{y}/\partial\bar{t}$, where $\bar{t} = t/T$ is the dimensionless time.

Substituting (3.1) into (3.2) and evaluating, we derive the following relations for the Reynolds and Strouhal numbers:

$$Re = \frac{\overline{U}\bar{c}}{\nu} = \frac{f R_g \bar{c}}{\nu}\int_0^1 \sqrt{\left(\frac{\partial\phi}{\partial\bar{t}}\right)^2 + \left(\frac{\partial\theta}{\partial\bar{t}}\right)^2}, \tag{3.3a}$$

$$St = \frac{f\bar{c}}{\overline{U}} = \frac{\bar{c}}{R_g}\frac{1}{\displaystyle\int_0^1 \sqrt{\left(\frac{\partial\phi}{\partial\bar{t}}\right)^2 + \left(\frac{\partial\theta}{\partial\bar{t}}\right)^2}}. \tag{3.3b}$$

Here $f = 1/T$ is the frequency, and ϕ and θ the three-dimensional kinematic angles for the displacement and deviation. From (3.3) it can be observed that the Reynolds number Re depends solely on the frequency f for given displacement $\phi(\bar{t})$ and deviation $\theta(\bar{t})$. The Strouhal number St does not vary independently. We fixed our Reynolds number at 110.

3.3. *Force and performance indicators*

The definition of the drag and lift forces is shown in figure 6. The lift is equal to the vertical force F_y, while the drag is taken equal to the horizontal force F_x, defined

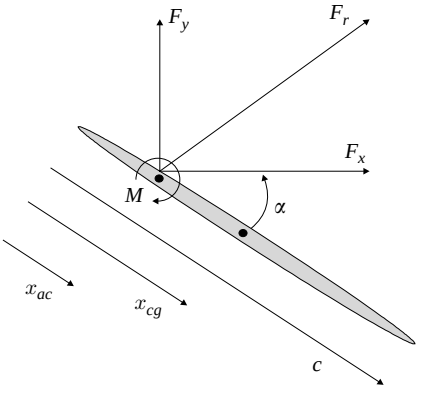

FIGURE 6. Forces on the wing.

positive in the positive x-direction. Commonly the forces are made dimensionless using the dynamic pressure based on the average velocity. With the strong variation in velocity, however, it is deemed more appropriate to scale the forces with the mean dynamic pressure itself. Hence, the forces are defined as

$$C_D = \frac{F_x}{\overline{q}\,\overline{c}}, \quad C_L = \frac{F_y}{\overline{q}\,\overline{c}}, \tag{3.4}$$

where C_D and C_L are the drag and lift coefficients. The mean dynamic pressure $\overline{q}$ is defined as

$$\overline{q} = \frac{1}{2}\rho\overline{U^2} = \frac{1}{2}\rho\frac{1}{T}\int_0^T \left(\left(\frac{\partial x}{\partial t}\right)^2 + \left(\frac{\partial y}{\partial t}\right)^2\right)\mathrm{d}t. \tag{3.5}$$

where the integration is evaluated over one flapping cycle. The force coefficients are the major parameters used to assess the influence of the different wing motion models. In addition, the ratio between the time-averaged lift coefficient, $\overline{C_L}$, and the time-averaged drag coefficient, $\overline{C_D}$, is used to characterize performance. These force averages are obtained by integration of C_L and C_D. The lift is averaged over the complete period, while for the drag the averages are per half-stroke. The average lift-to-drag ratio, $(\overline{C_L}/\overline{C_D})_{ave}$ is chosen as an indicator of aerodynamic performance, also known as the glide number in aerospace engineering. Since the average lift coefficients of the different kinematic models are matched, the lift-to-drag ratio is corrected for any differences in lift. Therefore, a high lift-to-drag ratio effectively means low drag at equal lift.

3.4. *Different wing kinematic models*

Since the main purpose of this study is to investigate the influence of wing kinematics on the aerodynamic performance during hovering fruit fly flight, four different kinematic models, with different degree of complexity, have been analysed. Two of these models, the pure harmonic motion and the Robofly experimental kinematics, have appeared in the literature. The third model represents the actual fruit fly kinematics as observed in experiments and the last one was a modification of the latter, chosen to investigate the effect of symmetry in the wing motion.

In order to facilitate the comparison the model parameters are chosen based on matching the mean quasi-steady lift coefficient, see Appendix A. Although according to Sane & Dickinson (2001) the mean drag is strongly influenced by the unsteady flow physics, which are not fully present in the quasi-steady theory, the mean lift coefficient

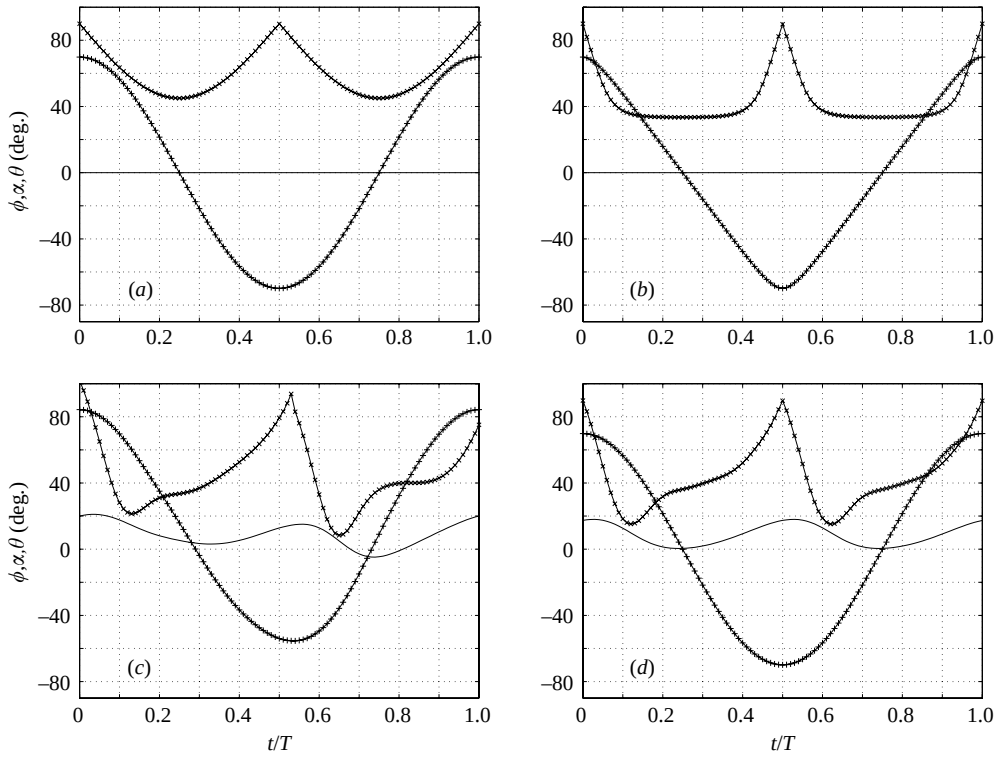

FIGURE 7. Kinematic angles of the different kinematic models. (*a*) Harmonic model, (*b*) Robofly model, (*c*) fruit fly model, (*d*) simplified fruit fly model. +, displacement; ×, angle of attack; —, deviation.

is predicted well using this theory. Using quasi-steady theory we constructed the different kinematic models such that their quasi-steady lift coefficients are matched within 1 %. For the symmetric models this force is equal to the resultant force. In view of the limitations of the quasi-steady theory, the difference between predicted and simulated values is expected to exceed this 1 % tolerance. However, in § 4 we will show that the computed mean lift coefficients of our numerical simulations are reasonably well matched for all models, which provides an *a posteriori* justification of our choices for the model parameters.

The characteristic kinematic shapes of each model are described and then used in § 4 to investigate the influence of the models on the force histories and the performance. Analysing those aspects leads to a better understanding of how the fruit fly may have kinematic features which are absent in the simpler models, and reveals the relevance of including these features in theoretical models.

The first of the four models is described by pure sine and cosine functions and will therefore be referred to as the harmonic model (see Wang *et al.* 2004). The displacement, angle of attack and deviation, are shown in figure 7(*a*).

The second model takes the wing kinematics as used in the Robofly model (Dickinson *et al.* 1999). In figure 7(*b*) it is shown that the flip from down-to upstroke is postponed to the end of the translational phase, which results in the 'sawtooth' shape of the displacement. Large accelerations at stroke reversal are the result. The deviation is zero, just as in the harmonic model.

The third model, shown in figure 7(*c*), is derived from measurements on real fruit flies (Fry *et al.* 2003) and is therefore considered as the most realistic fruit fly kinematic model. This model includes the deviation, which results in a 'figure-of-eight' pattern. Neither the displacement, angle of attack nor deviation is symmetric during the flapping period.

In order to investigate the fact that the observed fruit fly kinematics lacks an exact symmetry in the wing stroke pattern, a symmetrical model was constructed, referred to as the symmetric fruit fly model, displayed in figure 7(*d*). Within this model the motion is identical for the downstroke and upstroke. Like the realistic fruit fly model this symmetric model includes a time-dependent deviation such that the observer sees a 'figure-of-eight' pattern of the wing. Neither of those last two realistic kinematic models can be described using simple analytical functions without losing significant information. When comparing the motion parameters, ϕ, α and θ, for each model it becomes possible to identify certain important differences. The Robofly initially has a larger gradient in time of the angle of attack compared to the harmonic case (figure 7*a*, *b*). During translation from about $t = 0.1T$ to $t = 0.4T$ the angle of attack flattens at a value of almost 40°. This trapezoidal shape of α is characteristic for the Robofly and may be influencing the performance. Although the Robofly model clearly shows similarities with the fruit fly models the latter has some typical additional features, the most obvious being the extra 'bump' in angle of attack just after stroke reversal, compared to the Robofly (figure 7*b*, *c*): it follows the same high angular velocity, but instead of flattening, the fruit fly wing α descends to the 'bump'. After the 'bump' the angle of attack more or less matches the plateau found in the Robofly but starts to increase earlier. During stroke reversal the gradient of α matched the harmonic model closer than the Robofly with its high gradients.

The harmonic and Robofly models lack deviation, so no 'figure-of-eight' is present. The deviation of the fruit fly model is asymmetric during the complete cycle, but also during each half-stroke (figure 7*c*). This is likely to influence the performance since the effective angle of attack is altered due to deviation. It is also observed that the deviation is negative for a period during the upstroke. Therefore the deviation of the realistic fruit fly is averaged to derive the simplified fruit fly model (figure 7*d*). This last model is used to investigate the influence of deviation on the force histories and performance.

4. Results and discussion

In the previous section it was observed that the most interesting aspects of the Robofly kinematic model are the 'sawtooth' displacement and the trapezoidal angle of attack. This implies that strong translational and rotational accelerations occur at stroke reversal. The more realistic fruit fly models are characterized by a 'bump' in angle of attack and the presence of deviation. We present results of two comparative studies. The first is an overall comparison of the complete kinematic models, which is described in § 4.1. In the second the effect of the characteristic features identified above are considered more in detail. In order to assess the effect of these kinematic features in isolation, the comparison is made using the simplest model, the harmonic model, as baseline; this baseline model is subsequently modified by adding respectively the sawtooth displacement, trapezoidal angle of attack, extra bump in angle of attack and the presence of deviation. The results of this comparison, in terms of vortex dynamics, as well as the resulting lift and drag histories are studied in § 4.2.

Kinematic model	$\overline{C_L}$	$\overline{C_{D\,downstroke}}$	$-\overline{C_{D\,upstroke}}$	$\overline{C_L}/\overline{C_{D\,ave}}$
Harmonic	1.483 (−3.7 %)	1.848	1.839	0.805 (−29 %)
Robofly	1.417 (−8.0 %)	2.466	2.448	0.577 (−49 %)
Realistic fruit fly	1.540 (baseline)	1.387	1.335	1.132 (baseline)
Simplified fruit fly	1.454 (−5.6 %)	1.012	1.596	1.115 (−1.5 %)

TABLE 1. Time-averaged force coefficients using the complete models.

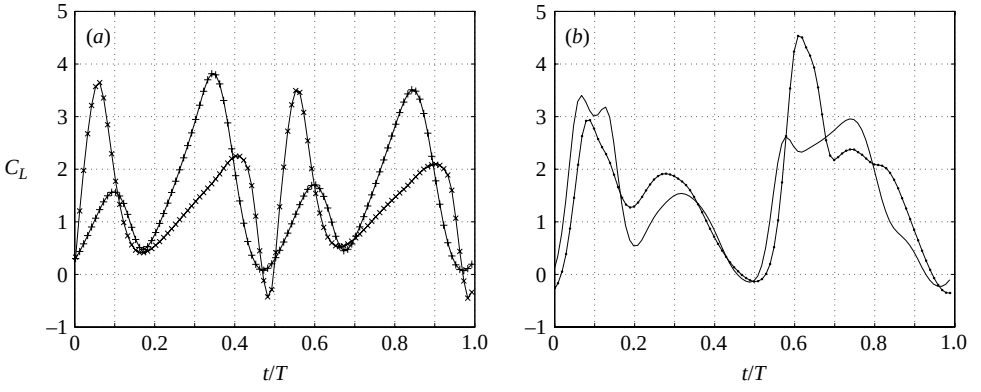

FIGURE 8. Lift force histories of the baseline kinematic models: +, harmonic model; ×, Robofly model; ●, realistic fruit fly model; −, simplified fruit fly model.

4.1. *Overall model comparison*

In table 1 the mean force coefficients are given for the four models: the harmonic model, the Robofly model, the realistic fruit fly model and the simplified fruit fly model. The mean drag, for each half-stroke, and lift coefficients are given, as well as the average lift-to-drag ratio, which characterizes aerodynamic performance.

The differences in the obtained mean lift coefficients are significantly smaller than the differences in lift-to-drag ratios. Therefore the conclusions on the performance comparison are considered to be significant. The lift force histories are shown in figure 8.

The mean drag for the harmonic and Robofly models is substantially higher compared to the fruit fly models. This is also illustrated in figure 9 (drag history) and figure 10 (force vectors). Figure 11 shows the vorticity contours of the realistic fruit fly model compared with the harmonic model. It can be seen in figure 7(*a*) that the effective angle of attack is higher in the harmonic case, compared to the realistic fruit fly model, figure 7(*c*). Therefore the mean drag contribution of the leading-edge vortices (LEV) is higher. The decrease in effective angle of attack in the realistic fruit fly model is also enlarged by the presence of the bump. This drag-increasing effect is even larger for the Robofly model due to the trapezoidal angle of attack. The sawtooth-shaped Robofly displacement could play an important role as is discussed in the next section. The different kinematic patterns are also illustrated in figure 10, which shows the resultant force vectors during a full stroke for the baseline kinematic models.

The mean drag coefficient of the simplified fruit fly is not symmetric, i.e. the drag during the upstroke is about 57 % higher than during the downstroke, which is attributed to the complex vortex dynamics. Nevertheless, the average value during a

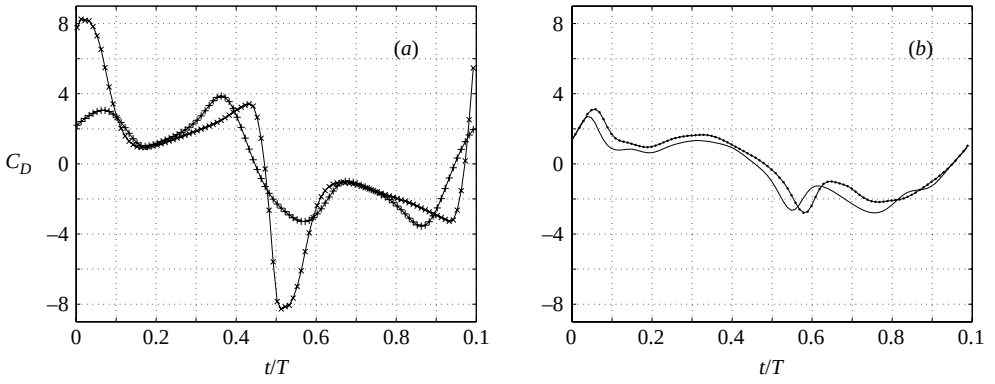

FIGURE 9. Drag force histories of the baseline kinematic models; +, harmonic model; ×, Robofly model; ●, realistic fruit fly model; —, simplified fruit fly model.

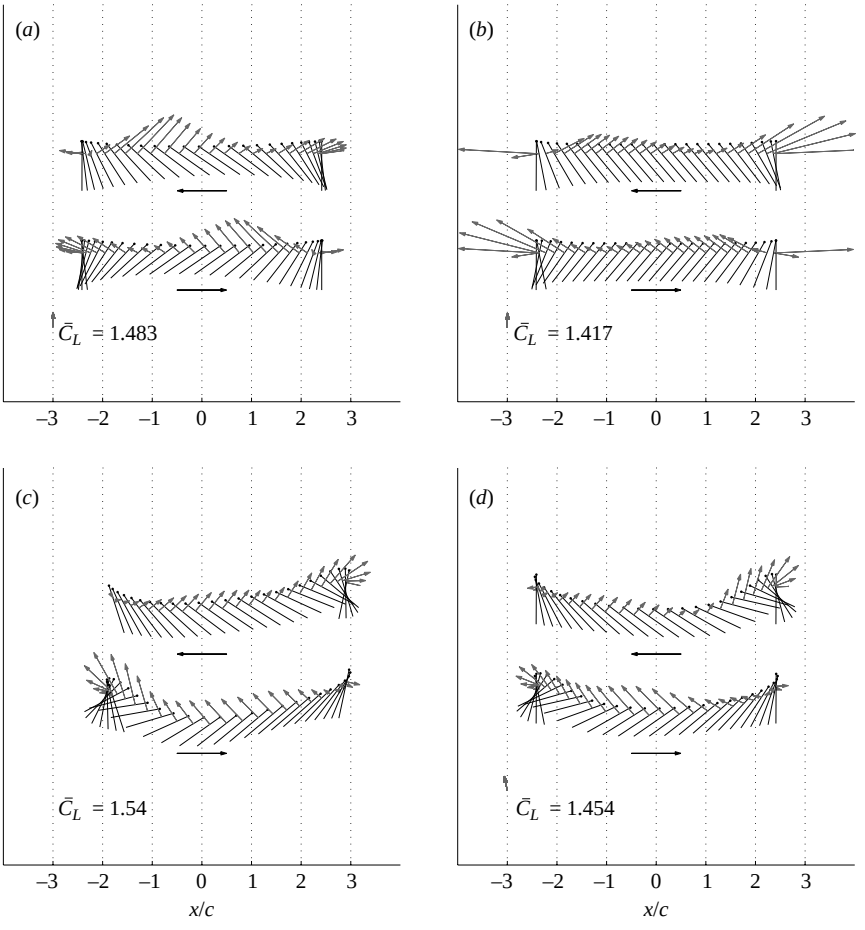

FIGURE 10. Force vectors during each half-stroke. (*a*) harmonic model, (*b*) Robofly model, (*c*) realistic fruit fly model, (*d*) symmetric fruit fly model.

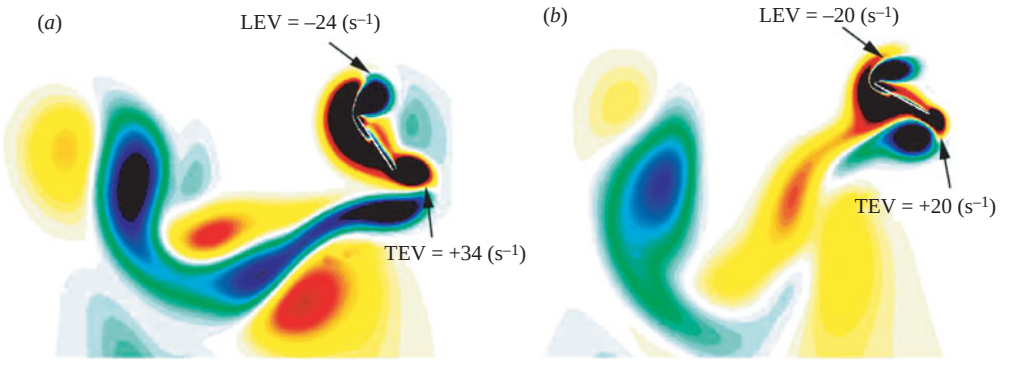

FIGURE 11. Vorticity contours at $t = 0.1T$ (blue: clockwise, corresponding to negative vorticity values) (*a*) harmonic model, (*b*) realistic fruit fly model. LEV denotes leading-edge vortex and TEV trailing-edge vortex.

complete stroke matches the mean drag coefficient obtained with the realistic fruit fly model.

When comparing the lift-to-drag ratios in table 1 it can be observed that within the model assumptions, the fruit fly models perform better than the less complex models. Compared to the harmonic model the realistic fruit fly model shows a significant decrease in drag of 29 % at comparable lift. The difference with the Robofly model is even larger, 49 %. These performance increases are the result of the lower drag coefficients in both fruit fly models due to certain beneficial kinematic features. The current results provide insight into the effects of some of these kinematic features. However, one has to be cautious when extrapolating these results to real flies since in reality not every flapping period displays exactly the same kinematic profile. Next, the individual influences of different kinematic shapes are studied.

4.2. *Kinematic features*

4.2.1. *Influence of sawtooth displacement used by the Robofly*

The sawtooth-shaped displacement of the Robofly is investigated in isolation to assess its influence on the force histories and the aerodynamic performance. We therefore appended to the purely harmonic model the Robofly displacement and compared the results with those obtained using the original harmonic model. Figure 12(*a*) shows the force vectors acting on the wing during the up- and downstroke. In addition, the force histories during one full stroke are shown in figure 13. From figure 13 it is observed that to the global force histories look similar the harmonic model. Two force peaks are observed close to $t = 0.1T$ and $t = 0.4T$, respectively, which are repeated since the motion is symmetric. The lift peaks are almost equal but the drag peaks are significantly larger for the sawtooth case, see figure 13(*b*). This also explains the larger mean drag compared to the harmonic model which can be seen in table 2.

In figures 14(*a*) and 14(*b*) the vorticity contours are plotted at $t = 0.1T$ for the harmonic model and the one with the appended sawtooth-shaped displacement. It can be seen that the LEV is stronger for the sawtooth case which explains the higher drag peak. The stronger LEV at the beginning of the downstroke in the sawtooth case is most likely caused by the higher velocity gradient. This leads to a larger shear layer forming a stronger vortex. On the other hand, at the end of the half-stroke the wing decelerates faster in the sawtooth case which results in a weaker LEV. Since the

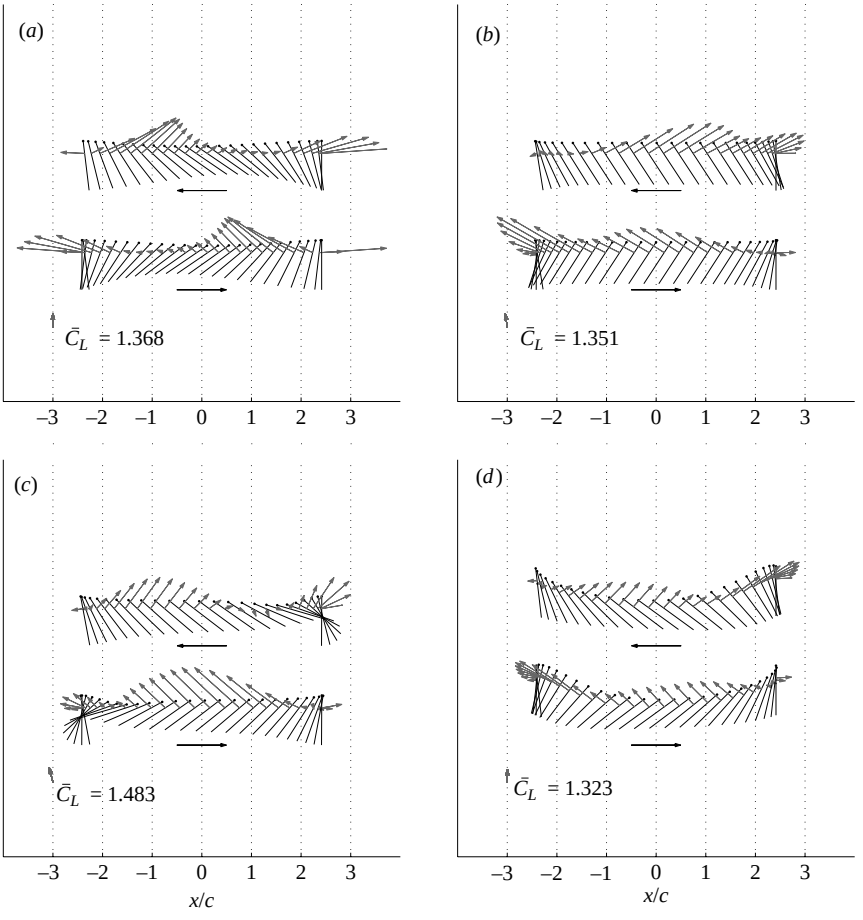

FIGURE 12. Force vectors during each half-stroke. (*a*) harmonic model with sawtooth ϕ, (*b*) harmonic model with trapezoidal α, (*c*) harmonic model with extra bump α, (*d*) harmonic model with deviation θ.

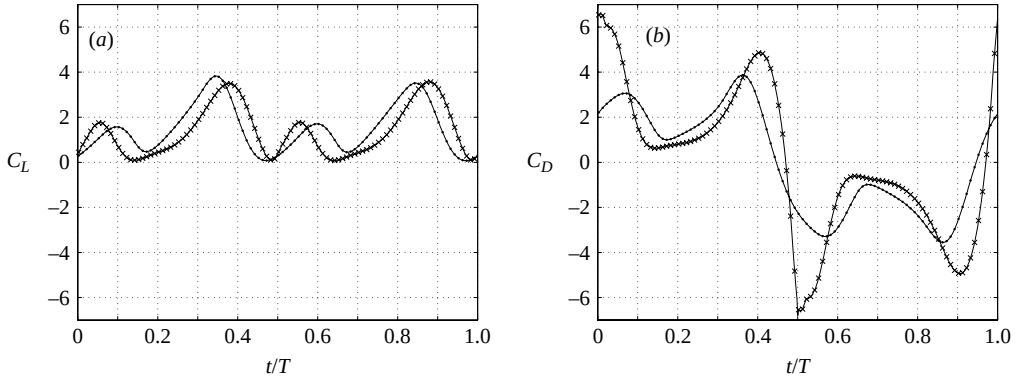

FIGURE 13. Force histories to investigate the influence of the sawtooth displacement compared to the harmonic model: ●, harmonic ϕ, α, θ; ×, harmonic α, θ and Robofly ϕ.

Kinematic model	$\overline{C_L}$	$\overline{C_{Ddownstroke}}$	$-\overline{C_{Dupstroke}}$	$\overline{C_L}/\overline{C_{Dave}}$
harm. ϕ, α and θ	1.483 (baseline)	1.848	1.839	0.804 (baseline)
harm. α, θ + Robofly ϕ	1.366 (−7.9 %)	2.240	2.250	0.608 (−24.3 %)
harm. ϕ, θ + Robofly α	1.351 (−8.9 %)	2.302	2.733	0.537 (−33.3 %)
harm. ϕ, θ + simp. fruit fly. α	1.483 (0.0 %)	1.221	1.969	0.930 (+15.6 %)
harm. ϕ, α + simp. fruit fly. θ	1.323 (−10.8 %)	1.807	1.776	0.738 (−8.2 %)

TABLE 2. Time-averaged force coefficients to investigate the influence of kinematic shapes. Each characteristic shape is varied with respect to the harmonic motion model.

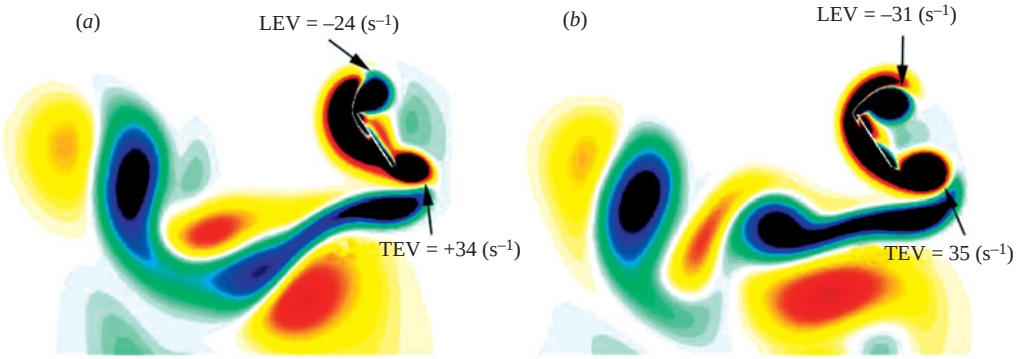

FIGURE 14. Vorticity contours at $t = 0.1T$ (blue: clockwise, corresponding to negative vorticity values): (*a*) harmonim model, (*b*) harmonic model with sawtooth displacement.

wing orientation is almost vertical, at $t = 0.1T$ the drag peak is larger than the lift peak.

The larger mean drag is reflected in the integrated values in table 2. Due to this larger drag during each stroke, the sawtooth-shaped displacement leads to a lower lift-to-drag ratio, which shows a decrease of 24.3 % with respect to the harmonic case.

4.2.2. *Influence of the trapezoidal angle of attack used by the Robofly*

In combination with the sawtooth displacement, the Robofly uses a trapezoidal shape for the angle of attack. In order to determine the effect of this shape the harmonic model is extended to include this trapezoidal angle of attack. The results are compared with those obtained with the original harmonic model, see figure 12(*b*) for the force vectors. The lift and drag coefficients are plotted in figure 15. An unexpected observation is the asymmetry in the force distribution for the trapezoidal angle of attack despite the symmetry of the kinematics. This leads to the non-zero mean horizontal force along a complete stroke cycle. Although this model is symmetric, the force distributions are not, since the complex vortex dynamics are nonlinear and asymmetric.

From figure 15 it is clear that at the beginning of a stroke the lift peak of the trapezoidal case is larger. In figure 16 this is illustrated at the beginning of the upstroke using vorticity contours. The LEV is larger in case of the trapezoidal angle of attack. This can be explained as follows. In the trapezoidal case the wing reaches the maximum angle of attack earlier in the stroke, see figure 12(*b*). Therefore the angle of attack is larger at the early start of a stroke compared to the harmonic

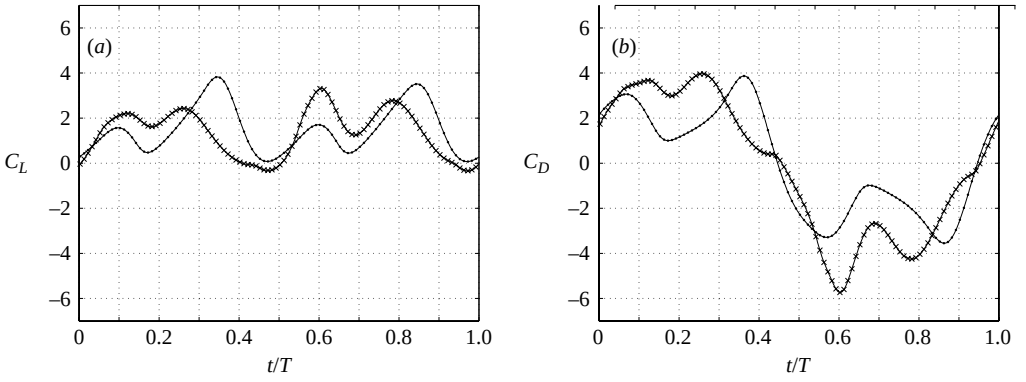

FIGURE 15. Influence of the trapezoidal angle of attack compared to harmonic model: ●, harmonic ϕ, α, θ; ×, harmonic α, ϕ and Robofly α.

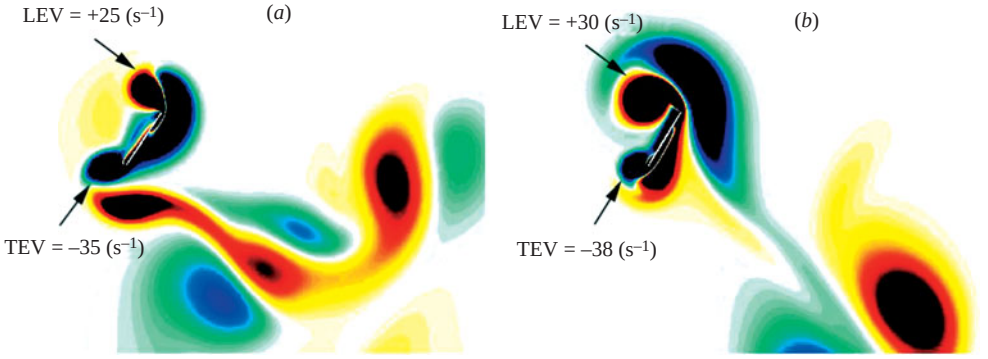

FIGURE 16. Vorticity contours at $t = 0.6T$ (blue: clockwise, corresponding to negative vorticity values): (*a*) harmonic model, (*b*) harmonic model with trapezoidal α.

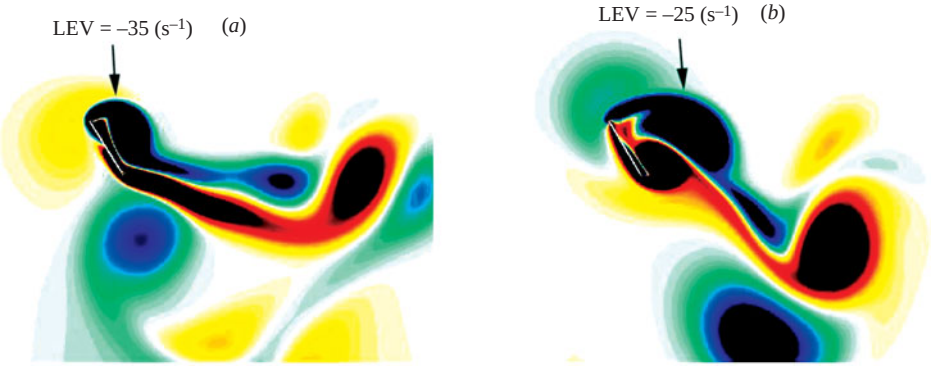

FIGURE 17. Vorticity contours at $t = 0.4T$ (blue: clockwise, corresponding to negative vorticity values): (*a*) harmonic model, (*b*) harmonic model with trapezoidal α.

model. Since large angle of attacks cause high velocity gradients over the leading edge, larger vortices occur at the beginning of a stroke.

Another interesting result is the low second peak in the lift, at the end of each stroke, compared to the harmonic model. From figure 17(*b*), one observes stronger

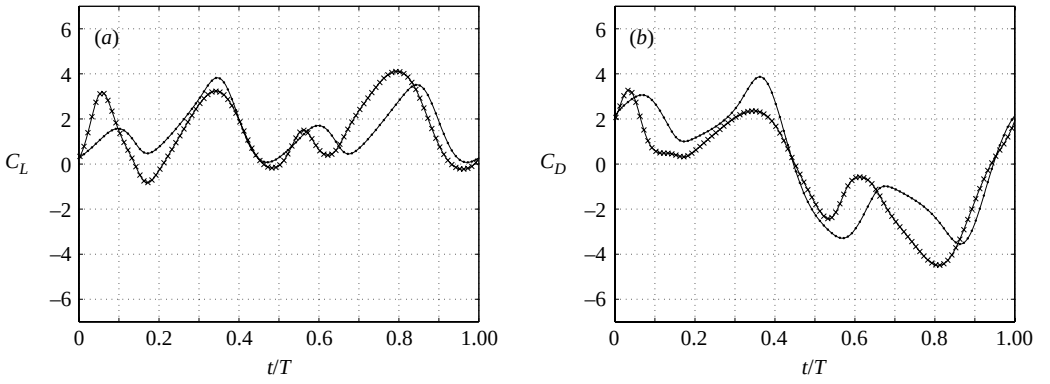

FIGURE 18. Influence of the extra bump in angle of attack: ●, harmonic ϕ, α, θ; ×, harmonic α, ϕ and fruit fly α.

and more pronounced vortices in the wake of the trapezoidal case. This could indicate a larger amount of vortex shedding during the period when the angle of attack is nearly constant. This results in a lower second peak since the LEV has decreased in size and strength. Altogether, the mean lift is slightly decreased whereas the mean drag is increased. This leads to a significant performance decrease of 33.3 % due to the trapezoidal angle of attack variation, see table 2.

4.2.3. *Influence of the extra bump in angle of attack used by the fruit fly*

The fruit fly models have an extra bump in angle of attack. To allow comparison the symmetric bump variation in the simplified fruit fly model is used to compare results with the harmonic model. Figure 12(*c*) shows the force vectors during up- and downstrokes. In figure 18 the lift and drag forces are shown for the harmonic model with and without the symmetric bump in angle of attack. From table 2 it is seen that with this feature the mean lift does not change much. However, the drag during the downstroke is significantly affected. A decrease of at least 30 % in mean drag is found, compared to the harmonic case. It is also noted that there are asymmetric force distributions as was the case when using the trapezoidal angle of attack. On the other hand the drag is slightly increased during the upstroke such that the mean lift-to-drag ratio is still increased by more than 15.6 %. From figure 18 it is observed that the extra bump generates an extra lift peak at the beginning of the downstroke. When figures 19(*a*) and 19(*b*) are compared, the decrease in effective angle of attack as a result of the bump is seen to be considerable compared to the harmonic case. The same was found for the Robofly case. Therefore, for the case with the bump in angle of attack, the LEV provides almost exclusively lift since the wing orientation is nearly horizontal. This is also the main reason for the lower drag during downstroke.

Figure 20 shows the vorticity at the beginning of the upstroke at the time of the 'bump'. The LEV is larger without than with the bump in angle of attack. This causes a loss in lift just after stroke reversal with the bump in angle of attack compared to the harmonic model.

4.2.4. *Influence of wing deviation used by the fruit fly*

The last important characteristic of the kinematics is the deviation, present in the realistic and simplified fruit fly model. This deviation causes a 'figure-of-eight' pattern to be described by the wing tip instead of motion solely in the stroke plane. Since deviation could introduce a large velocity component perpendicular to the stroke

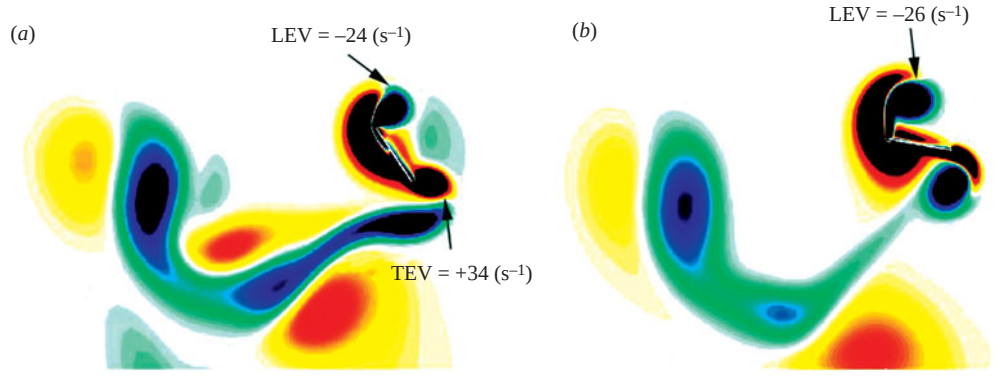

FIGURE 19. Vorticity contours at $t = 0.1T$ (blue: clockwise, corresponding to negative vorticity values): (a) harmonic model, (b) harmonic model with extra bump in α.

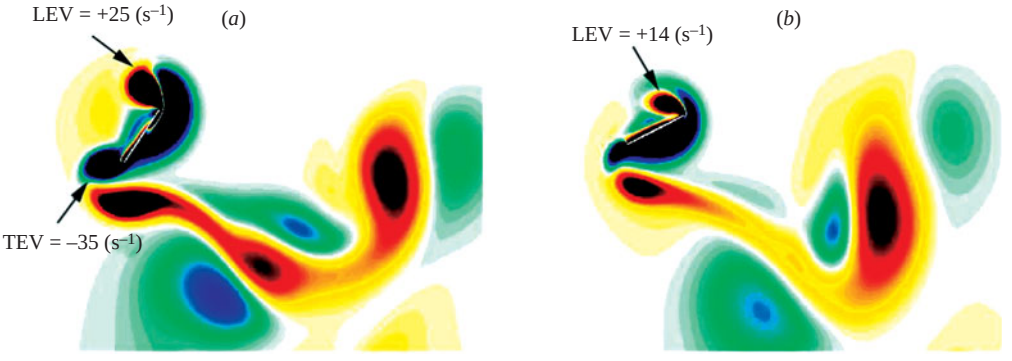

FIGURE 20. Vorticity contours at $t = 0.6T$ (blue: clockwise, corresponding to negative vorticity values): (a) harmonic model, (b) harmonic model with extra bump in α.

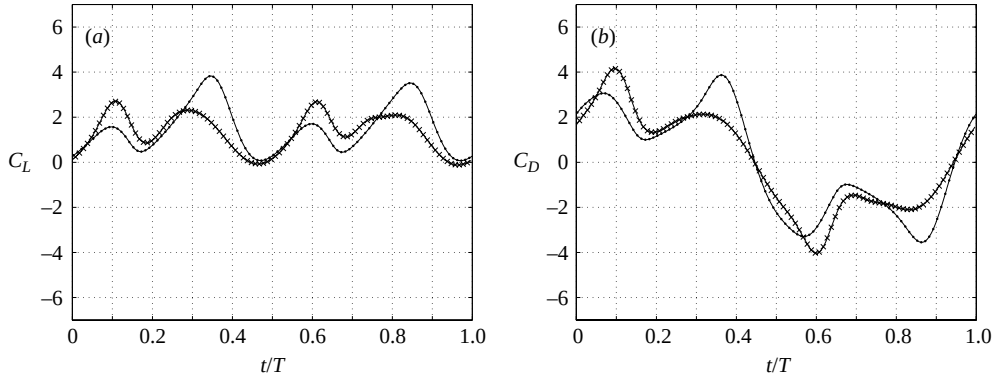

FIGURE 21. Influence of the deviation compared to the harmonic model: ●, harmonic ϕ, α, θ; ×, harmonic α, α and fruit fly θ.

plane, the effective angle of attack is highly affected. This motion perpendicular to the stroke plane is illustrated in figure 12(d) which also shows the force vectors.

Figure 21 shows the force coefficients during one flapping period with deviation added to the harmonic model. The mean lift and drag are not strongly influenced by

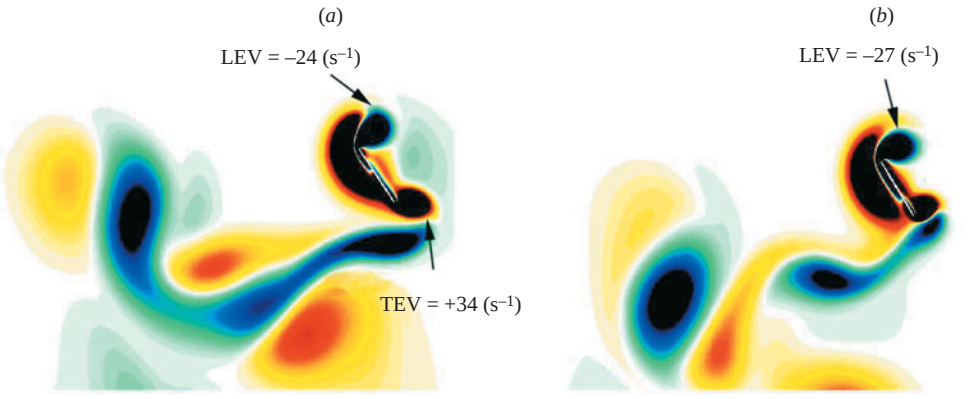

FIGURE 22. Vorticity contours at $t = 0.1T$ (blue: clockwise, corresponding to negative vorticity values): (*a*) harmonic model, (*b*) harmonic model with deviation.

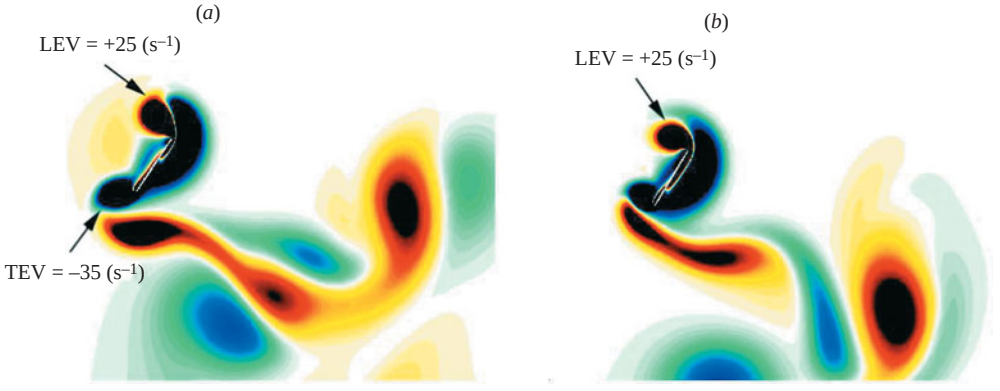

FIGURE 23. Vorticity contours at $t = 0.6T$ (blue: clockwise, corresponding to negative vorticity values): (*a*) harmonic model, (*b*) harmonic model with deviation.

the deviation, see table 2. The mean lift is decreased by 10.8 % and the mean drag is almost unaffected by the presence of deviation, about 2 % – 4 % difference in both strokes. It is also seen that the force distributions remain symmetric.

The large influence of the deviation on the variation of the lift force is observed at the start ($t = 0.1T$ and $t = 0.6T$) and end ($t = 0.4T$ and $t = 0.9T$) of each stroke. Just after stroke reversal a lift peak occurs, which is higher compared to the harmonic case. On the other hand, at the end of each stroke the harmonic lift peak was decreased by the deviation. It appears that the force distribution is levelled or balanced by the deviation.

The flow dynamic mechanism for this is shown in the vorticity visualizations at the beginning of the stroke shown in figure 22. Compared to the harmonic model, the deviation causes a slightly stronger LEV at $t = 0.1T$. The influence of the deviation is quite large since the deviation increases the effective angle of attack considerably just after stroke reversal. At the end of a stroke the wings move up again which leads to a decrease in effective angle of attack. Figure 23(a, b) shows LEVs of comparable strength for both cases.

Summarizing, the deviation levels the force distributions while the mean lift and drag are almost unaffected. This leads to the suggestion that a fruit fly may use the

deviation to level the wing loading over a flapping cycle. Three-dimensional studies are needed to investigate to what extent this effect is present in real insect flight.

5. Conclusions

The effect of wing motion kinematics on the aerodynamic characteristics of hovering insect flight was investigated by means of two-dimensional numerical flow simulations. The results of the present two-dimensional study may provide useful insights into real three-dimensional insect flight (Wang *et al.* 2004).

Four different kinematic models, with different complexity, have been analysed using two-dimensional time-dependent Navier–Stokes simulations. Two of these models, pure harmonic motion and the Robofly experimental kinematics, have appeared in the literature. The third model represents actual fruit fly kinematics as observed in experiments and the last one was a modification of the latter, chosen to investigate the effect of symmetry. The most prominent aspects of the Robofly kinematic model are the sawtooth displacement and the trapezoidal angle of attack. The fruit fly models are characterized by a bump in angle of attack and the presence of deviation. To facilitate the comparison these models are dynamically scaled at $Re = 110$ and constructed such that their mean quasi-steady lift coefficient was matched.

It was found that the realistic fruit fly wing kinematics result in significantly lower drag at similar lift compared with the simplified wing kinematic models used in the literature. The result that the fruit fly kinematics increases aerodynamic performance agrees with the predictions of the quasi-steady theory, see Appendix A, but the numerical flow simulations provide a more complete quantitative analysis of the flow behaviour. To investigate which aspects of the kinematic shapes are the most important they were compared to the harmonic model.

First an overall comparison of the complete kinematic models was given. It was shown that the difference in performance in terms of mean lift-to-drag ratio between the different kinematic models was significant. The mean aerodynamic drag at equal lift of the fruit fly models is about 49 % lower compared to the Robofly model and about 29 % lower with respect to the harmonic model. Therefore the effect of the characteristic features has been studied: the harmonic model was extended by respectively the sawtooth displacement, trapezoidal angle of attack, extra bump in angle of attack and the presence of deviation. The vortex dynamics, as well as the resulting lift and drag histories, were studied.

The results showed that the sawtooth amplitude used in the Robofly model has a small effect on the mean lift but the mean drag is affected significantly. Due to the high acceleration during stroke reversal of the sawtooth-shaped amplitude, the mean drag at comparable lift is increased by 24.3 %. The second model simplification used by the Robofly, the trapezoidal angle of attack, caused the LEV to separate during the translational phase. This led to an increase in mean drag during each half-stroke. Also in this case large accelerations at stroke reversal lead to a decrease in lift-to-drag ratio of 33.3 %.

The extra bump in angle of attack in the fruit fly model does not affect the mean lift to a large extent. During the beginning of the up- and downstroke the bump decreases the angle of attack such that the wing orientation is almost horizontal. This leads to a significant decrease in drag which improves aerodynamic performance in the sense of lift-to-drag ratio by 15.6 %. The other realistic kinematic feature is the deviation, which is found to have only a marginal effect on the mean lift and mean

Kinematic model	$\overline{C_{Lquasi}}$	$\overline{C_{Dquasi}}$	$\overline{C_L}/\overline{C_{Dave}}$
Harm. ϕ, α and θ	1.444	2.145	0.673
Harm. α, θ + Robofly ϕ	1.444	2.145	0.673
Harm. ϕ, θ + Robofly α	1.444	2.597	0.556
Harm. ϕ, θ + simp. fruit fly α	1.483	1.708	0.868
Harm. ϕ, α + simp. fruit fly θ	1.329	1.886	0.705

TABLE 3. Time-averaged quasi-steady values for both lift and drag forces.

drag. However, the effective angle of attack is altered such that the deviation leads to levelling of the force distribution.

The results from the present study show that special features of insect flight need to be included to increase the accuracy of performance models of insect flight. In particular they indicate that kinematic features, found in fruit fly kinematics, like the extra bump in angle of attack and deviation, may lead to drag reduction compared to harmonic kinematics. Although the present study is restricted to a two-dimensional flow model, it provides insight into the importance of kinematic features in insect aerodynamics. Three-dimensional studies need to be performed to further investigate to what extent the present results are important for our understanding of insect flight.

This research is supported by the Dutch Organisation for Scientific Research, NWO-ALW grant 814.02.019. D. L. thanks Rosalyn Sayaman for help with the analysis of fruit fly kinematics. D. L. is supported by NWO-ALW grant 817.02.012.

Appendix A. Force prediction according to quasi-steady theory

Quasi-steady theory was first applied by Weish-Fogh & Jensen (1956) to calculate the force history of tethered locusts. In this theory the forces are determined at each instant by defining an equivalent steady problem. Later Dickinson & Götz (1993) used rigid wings starting from rest at $Re = 192$. More recently Dickinson *et al.* (1999) employed the Robofly at $Re = 79 - 236$ to create polar plots which could be fitted by the following empirical relations:

$$C_L = 0.225 + 1.58 \sin(2.13\alpha - 7.20), \tag{A 1a}$$

$$C_D = 1.920 - 1.55 \cos(2.04\alpha - 9.82), \tag{A 1b}$$

where α is the effective angle of attack.

Since we used their three-dimensional Robofly model to derive our kinematic models, equations (A 1) are used to create a framework of comparison for the results obtained with the different kinematic models. The parameters of the model are chosen such that the mean quasi-steady lift coefficient is the same for all kinematic models used.

Table 3 shows the quasi-steady values for the average lift and drag. Compared to table 2 the lift is described well by quasi-steady theory. On the other hand, quasi-steady theory is insufficient to accurately describe the drag, which confirms the need for accurate numerical simulations.

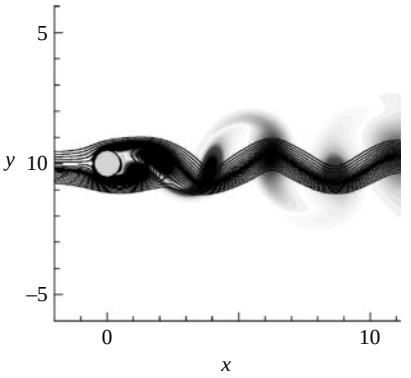

FIGURE 24. General unsteady flow around a fixed cylinder, $Re = 150$. Vorticity contours are used to visualize the development of a von Kármán vortex street. Streamlines accentuate the wavy pattern in the vortex street.

Appendix B. Addition solver settings

For completeness we briefly describe the main settings of our code. The space discretization was second-order upwind and the time discretization was first-order implicit Euler (see Hirsch 1988), which is the only way the dynamic mesh module is implemented by Fluent. The pressure–velocity coupling in incompressible flow simulations was obtained using the iterative SIMPLEC scheme (Ferziger & Peric 2002) with under-relaxation coefficients for pressure, momentum and body forces equal to 0.8, 0.7 and 1.0. The accuracy was set to double-precision and the initial conditions were chosen to be uniform. The boundary condition on the body was set to no-slip. The convergence criterion for the iterative method was satisfied with mass and momentum residues decreasing by $O(10^{-4})$ in magnitude.

Appendix C. Validation using static and moving cylinders at lowRe

To validate the accuracy of our solver for highly unsteady and vortical flow, four validation test cases regarding flow around static and moving cylinders are defined. Because the main objective was simulating prescribed moving (translating and rotating) insect wings with large amplitudes it is important to represent the relevant flow physics in the test cases.

At low Reynolds numbers, in the range $100 \leqslant Re \leqslant 200$, the flow around following cases was used for validation: a static circular cylinder, a steady rotating cylinder, a rotationally oscillating cylinder and a transversally oscillating cylinder. In all four test cases the Reynolds number is defined as $Re = U_{ref}L/\nu$. Here U_{ref} is chosen equal to the free-stream velocity and L equal to the cylinder diameter. The main parameter selected for comparison is the average drag coefficient, which is well-documented in literature.

The first case concerns the flow around a static circular cylinder at $Re = 150$ where the flow is inherently laminar and unsteady, resulting in a periodic vortex wake. Henderson (1995) performed a spectral element numerical study which is used as the main reference for this case. Figure 24 shows the instantaneous vorticity contours for this case, which reveal the presence of the von Kármán vortex street behind the static cylinder. The corresponding $C_L - C_D$ limit cycles obtained on different mesh sizes $(12.5 \times 10^3 - 50 \times 10^3)$ are depicted in figure 25.

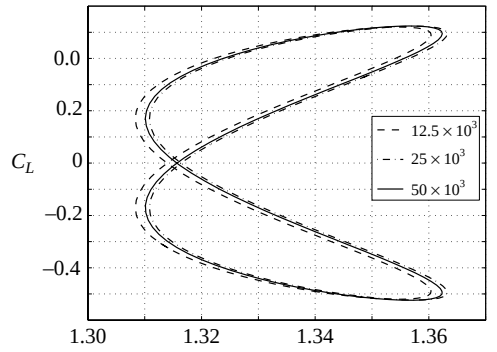

FIGURE 25. Phase Diagrams of unsteady flow around a static cylinder at $Re = 150$ and the corresponding limit cycles. The knot at $C_L = 0$ shifts to the left according to 25×10^3, 50×10^3 and 12.5×10^3 cells.

Case	Re	Motion parameters	References	$\overline{C_{Dref}}$	$\overline{C_D}$	Diff.
Static cylinder	150	–	Henderson (1995)	1.334	1.299	2.62 %
Const. rotation	100	$\omega L/U_{ref} = 2$	Stojkovic *et al.* (2002)	1.108	1.095	1.17 %
Rotational oscillating	200	$f_e = 0.18$, $A_m = 0.5$	Cheng *et al.* (2001)	1.650 ×	1.736 ×	5.2 % ×
Translational oscillating	185	$f_e = 0.154$, $A_e = 0.2L$	Guilmineau & Queutey (2002)	1.200 ×	1.251 ×	4.25 % ×

TABLE 4. Validation for the flow around static and moving circular cylinders. The difference (%) is with respect to the numerical value for that specific case found in the references.

Secondly, the numerical study performed by Stojkovic, Breuer & Durst (2002) is used to investigate the flow around a steady rotating cylinder at $Re = 100$. In this case the non-dimensional rotational velocity is defined as $L\omega/U_{ref}$, where ω is the constant angular velocity. Following Stojkovic *et al.* (2002) the Reynolds number and the rotation rate are respectively $Re = 100$ and $L\omega/U_{ref} = 2$.

Since the moving wing oscillates in a translational and rotational sense the flow around a rotational oscillating cylinder at $Re = 200$ is selected as the third test case. Cheng, Liu & Lam (2001) performed a numerical study and is used for this case. The rotational velocity is given by $u_b(t) = A_e \sin(2\pi f_e t)$. Here u_b is the oscillating velocity of the cylinder surface, A_e is the velocity amplitude and f_e the oscillating frequency. Corresponding to Cheng *et al.* (2001) the relevant parameters are chosen as follows: $Re = 200$, $A_e = 0.5$ and $f_e = 0.18$.

Finally a transversally oscillating cylinder at $Re = 185$ is investigated using the numerical study performed by Guilmineau & Queutey (2002). The plunging motion direction is perpendicular to the free-stream direction. The motion is defined as $y(t) = -A_e \sin(2\pi f_e t)$. Following Guilmineau & Queutey (2002) the relevant flow parameters are chosen to be $Re = 185$, $A_e = 0.2L$ and $f_e = 0.154$ which corresponds to 0.8 times the natural shedding frequency of a stationary cylinder at $Re = 185$. The amplitude of 0.2 times the cylinder diameter is relatively low to be relevant to insect aerodynamics but sufficient to investigate the moving wing capabilities of the numerical model.

The results of all four test cases are given in table 4 with a comparison based on the mean (time-average) drag value. It was found that concerning body conformal

$T/\Delta t$	Grid size $\times 10^3$	$\overline{C_L}$	Diff. (%)	$\overline{C_D}$	Diff. (%)
200	50	1.294	−8.09 %	2.086	−12.87 %
2000	50	1.496	baseline	2.394	baseline
20000	50	1.516	1.34 %	2.400	0.25 %
2000	25	1.330	−11.10 %	2.107	−11.99 %
2000	50	1.496	baseline	2.394	baseline
2000	100	1.509	0.87 %	2.415	0.88 %

TABLE 5. Verification using the flow around a harmonically moving wing. The influence of different grid sizes and time steps is investigated. The difference (%) is with respect to the 50×10^3 case with 2000 time steps.

moving meshes the computational model succeeds in simulating the validation cases: the mean drag coefficient deviates from the literature between 1.17 % and 5.2 % which is considered sufficiently accurate.

The errors for the third and fourth cases are somewhat larger (4 % − 5 %) than those for the first two cases, which is probably the result of the slightly higher Reynolds number $Re = 185 - 200$ for these cases. Although both the present and reference simulations consider laminar flow (which justifies the comparison) the actual flow in cases 3 and 4 may contain turbulent regions. The implication of this for the numerical simulations is likely to be an increased sensitivity to details and parameter settings of the different numerical studies, such as discretization schemes, iterative methods, mesh generation and time step size.

For the validation (cylinder) and verification (moving airfoil) studies we used mesh sizes of 12.5×10^3 (88×141), 25.000 (125×200), 50.000 (176×284) and 100.000 (250×400) cells. The first number in the brackets is the number of cells on the surface, whereas the second is the number of cells perpendicular to the surface. The time step for validation and verification was chosen such that the number of time steps within one vortex shedding cycle was 200, 2000 and 20000.

For the cylinder simulations the boundary condition at the far field Γ_3 was chosen to be velocity Dirichlet such that uniform-free-stream conditions are obtained.

For both cylinder and moving airfoil simulations mesh sizes of 12.5×10^3, 25×10^3, 50×10^3 and 100×10^3 are used, to verify grid convergence.

Appendix D. Verification using harmonic wing kinematics

In this verification study the translational amplitude was 4.2 wing chords and the rotational amplitude 45°. The frequency was chosen such that the Reynolds number based on the average velocity yields $Re = 110$.

In table 5 the average drag coefficients are shown for different grid sizes and time steps. When, for the baseline case with 50×10^3 cells, the temporal resolution is decreased from 2000 to 200 time steps the mean lift and drag coefficients become 8 % to 13 % lower. On the other hand, an increase in temporal resolution from 2000 to 20000 time steps led to negligible differences, i.e. less than 1.5 %.

Similar observations are made for the variation of the grid size. Coarsening from 50×10^3 to 25×10^3 cells, at a given time step, leads to a decrease of the lift and drag coefficients of almost 12 %, while refining from 50×10^3 to 100×10^3 gives very small differences, less than 1 %. Therefore we conclude that with our present solver

the choice 50×10^3 cells using 2000 time steps is sufficiently accurate and efficient to solve for moving insect wings in hovering flight.

REFERENCES

Birch, J. M. & Dickinson, M. H. 2003 The influence of wing-wake interactions on the production of aerodynamic forces in flapping flight. *J. Expl Biol.* **206**, 2257–2272.

Blondeaux, P., Fornarelli, F., Guglielmini, L., Triantafyllou, M. & Verzicco, R. 2005 Numerical experiments on flapping foils mimicking fish-like locomotion. *Phys. Fluids* **17**, 113601.

Bomphrey, R. J., Lawson, N. J., Taylor, G. K. & Thomas, A. L. R. 2006 Application of digital particle image velocimetry to insect aerodynamics: measurement of the leading-edge vortex and near wake of a hawkmoth. *Exp. Fluids* **40**, 546–554.

Brodsky, A. K. 1994 *The Evolution of Insect Flight*. Oxford University Press.

Cheng, M., Liu, G. & Lam, K. 2001 Numerical simulation of flow past a rotationally oscillating cylinder. *Computers & Fluids* **30**, 365–392.

Dickinson, M. H. 1994 The effects of wing rotation on unsteady aerodynamic performance at low Reynolds number. *J. Expl Biol.* **192**, 179–206.

Dickinson, M. H. & Götz, K. G. 1993 Unsteady aerodynamic performance of model wings at low Reynolds numbers. *J. Expl Biol.* **174**, 45–64.

Dickinson, M. H., Lehmann, F. & Sane, S. P. 1999 Wing rotation and the aerodynamic basis of insect flight. *Science* **284**, 1954–1960.

Dong, H., Mittal, R., Bozkurttas, M. & Najjar, F. 2005 Wake structure and performance of finite aspect-ratio flapping foils. *AIAA Paper* 2005-81.

Ellington, C. P. 1984 The aerodynamics of hovering insect flight. *Phil. Trans. R. Soc. Lond.* B **305**, 1–181.

Ellington, C. P., van den Berg, C., Willmott, A. & Thomas, A. 1996 Leading-edge vortices in insect flight. *Nature* **384**, 626–630.

Ferziger, J. & Peric, M. 2002 *Computational Methods for Fluid Dynamics*, 3rd edn. Springer.

Fry, S. N., Sayaman, R. & Dickinson, M. H. 2003 The aerodynamics of free-flight maneuvers in Drosophila. *Science* **300**, 295–298.

Guglielmini, L. & Blondeaux, P. 2004 Propulsive efficiency of oscillating foils. *Eur. J. Mech.* B/*Fluids* **23**, 255–278.

Guilmineau, E. & Queutey, P. 2002 A numerical simulation of vortex shedding from an oscillating circular cylinder. *J. Fluids Struct.* **16**, 773–794.

Henderson, R. D. 1995 Details of the drag curve near the onset of vortex shedding. *Phys. Fluids* **7**, 2102–2104.

Hirsch, C. 1988 *Numerical Computation of Internal and External Flows, Vol 1: Fundamentals of Numerical Discretization*. John Wiley & Sons.

Hover, F., Haugsdal, Ø. & Triantafyllou, M. 2004 Effect of angle of attack profiles in flapping foil propulsion. *J. Fluids Struct.* **19**, 37–47.

Isogai, K., Fujishiro, Saitoh, T., Yamamoto, M., Yamasaki, M. & Matsubara, M. 2004 Unsteady three-dimensional viscous flow simulation of a dragonfly hovering. *AIAA J.* **42**, 2053–2059.

Lentink, D. & Gerritsma, M. 2003 Influence of airfoil shape on performance in insect flight. *AIAA Paper* 2003-3447.

Lewin, G. & Haj-Hariri, H. 2003 Modelling thrust generation of a two-dimensional heaving airfoil in a viscous flow. *J. Fluid Mech.* **492**, 339–362.

Lighthill, M. 1969 Hydromechanics of aquatic animal propulsion. *Annu. Rev. Fluid. Mech.* **1**, 413–446.

Liu, H. & Kawachi, K. 1998 A numerical study of insect flight. *J. Computat. Phys.* **146**, 124–156.

Pedro, G., Suleman, A. & Djilali, N. 2003 A numerical study of the propulsive efficiency of a flapping hydrofoil. *Intl J. Numer. Meth. Fluids* **42**, 493–526.

Ramamurti, R. & Sandberg, W. 2002 A three-dimensional computational study of the aerodynamic mechanisms of insect flight. *J. Expl Biol.* **205**, 1507–1518.

Sane, S. P. & Dickinson, M. H. 2001 The control of flight force by a flapping wing: lift and drag production. *J. Expl Biol.* **204**, 2607–2626.

Sane, S. P. & Dickinson, M. H. 2002 The aerodynamic effects of wing rotation and a revised quasi-steady model of flapping flight. *J. Expl Biol.* **205**, 1087–1096.

Srygley, R. B. & Thomas, A. L. R. 2002 Unconventional lift-generating mechanisms in free-flying butterflies. *Nature* **420**, 660–664.

Stojkovic, D., Breuer, M. & Durst, F. 2002 Effect of high rotation rates on the laminar flow around a circular cylinder. *Phys. Fluids* **14**, 3160–3178.

Sun, M. & Tang, J. 2002 Unsteady aerodynamic force generation by a model fruit fly wing in flapping motion. *J. Expl Biol.* **205**, 55–70.

Wang, Z. J. 2000*a* Two dimensional mechanism for insect hovering. *Phys. Rev. Lett.* **85**, 2216–2219.

Wang, Z. J. 2000*b* Vortex shedding and frequency selection in flapping flight. *J. Fluid Mech.* **410**, 323–341.

Wang, Z. J., Birch, M. B. & Dickinson, M. H. 2004 Unsteady forces and flows in low Reynolds number hovering flight: two-dimensional computations vs robotic wing experiments. *J. Expl Biol.* **207**, 461–474.

Weish-Fogh, T. & Jensen, M. 1956 Biology and physics of locust flight. Basic principles of insect flight: a critical review. *Phil. Trans. R. Soc. Lond.* **239**, 415–458.

Williamson, C. H. K. 1995 Vortex dynamics in the wake of a cylinder. In *Fluid Vortices, Fluid Mechanics and its Applications* (ed. S. I. Green), chap 5. Kluwer.